Gypsum scaling in membrane distillation: Impacts of temperature and vapor flux

Kofi S.S. Christie [a], Thomas Horseman [b], Ruoyu Wang [a], Chunlei Su [a,c,d], Tiezheng Tong [e], Shihong Lin [a,b,*]

[a] Department of Civil and Environmental Engineering, Vanderbilt University, Nashville, TN 37235-1831, USA
[b] Department of Chemical and Biomolecular Engineering, Vanderbilt University, Nashville, TN 37235-1604, USA
[c] Beijing Engineering Research Centre of Process Pollution Control, Institute of Process Engineering, Chinese Academy of Sciences, Beijing 100190, China
[d] University of Chinese Academy of Sciences, Beijing 100049, China
[e] Department of Civil and Environmental Engineering, Colorado State University, Fort Collins, CO 80523, USA

HIGHLIGHTS

- The impacts of temperature and flux on gypsum scaling are experimentally decoupled.
- Interfacial saturation index alone cannot predict the onset of gypsum scaling.
- Temperature has a stronger impact than flux on critical water recovery.

ARTICLE INFO

ABSTRACT

Mineral scaling by sparingly soluble gypsum (CaSO$_4$•2H$_2$O) is a persistent challenge to membrane distillation (MD). The underlying relationship between the thermodynamic state of the precipitating solution and the point of flux decline due to rapid mineral growth remains unclear. In this work, a series of experiments along with a semi-empirical model are executed to examine the thermodynamic state of the feed solution at the feed/membrane interface to evaluate and compare the critical point of scaling. The experiments were deliberately designed in a way to decouple the influence of feed temperature and vapor flux. The thermodynamic state of the precipitating solution at the membrane interface is evaluated using the saturation index and the nucleation energy barrier derived from the chemical potential difference between the dissolved ions and the gypsum mineral. The model is rooted in established heat and mass transfer relationships and reflects the testing conditions used to carry out the experiments. The model is built upon experimental results across a range of operational conditions, with the bulk feed solution temperature ranging from 50 to 80 °C (at a constant flux) and the trans-membrane water flux ranging from 10 to 40 L m^{-2} h^{-1} (at a constant feed temperature). It was observed that interfacial saturation index calculated at the induction point was not consistent across different experiments, confirming that gypsum scaling in MD is controlled by kinetics instead of thermodynamics. We also found that temperature plays a more important role than vapor flux in affecting the critical recovery. Lastly, we also provide theoretical reasoning to support the experimental observation that gypsum scaling in MD is largely dominated by heterogeneous nucleation onto the membrane surface.

1. Introduction

Membrane distillation (MD) carries the potential to supplement the production of water sustainably by utilizing low-grade waste heat to treat brines resulting from water desalination and industrial processes [1]. MD is especially promising for applications in which the feed solution salinity exceeds the maximum treatment range for reverse osmosis (RO), which is about 80 g L^{-1} [2], or when the target treatment capacity is too small to justify multi-stage flash distillation and multi-effect distillation [3]. Improvements in the energy efficiency of modular MD processes and the development of robust MD membranes

---

Nomenclature

CP	concentration polarization
CPC	concentration polarization coefficient
IAP	ion activity product
MD	membrane distillation
RO	reverse osmosis
SI	saturation index
TP	temperature polarization
TPC	temperature polarization coefficient

Symbols

a_i	Nusselt coefficient of solution i
A	Arrhenius constant (s^{-1})
A_m	active area of membrane (m^2)
A_S	surface area of a nucleating cluster (m^2)
b_i	Nusselt coefficient of solution i
C_b	bulk feed solute concentration (mmol L^{-1} or mol L^{-1})
c_i	Nusselt coefficient of solution i
C_m	interfacial feed solute concentration (mmol L^{-1} or mol L^{-1})
$C_{m,\,0}$	initial interfacial feed solute concentration (mmol L^{-1} or mol L^{-1})
C_m^*	critical interfacial feed solute concentration (mmol L^{-1} or mol L^{-1})
$C_{p,\,i}$	specific heat capacity of solution i (J g^{-1} K^{-1})
d	hydraulic diameter of flow channel (m)
E_a	activation energy (J mol^{-1})
ΔG	nucleation work (J)
ΔG_{het}^*	critical heterogeneous energy barrier for nucleation (kJ mol^{-1})
ΔG_{hom}^*	critical homogeneous energy barrier for nucleation (kJ mol^{-1})
h_d	distillate solution heat transfer coefficient (W m^{-2} K^{-1})
h_f	feed heat transfer coefficient (W m^{-2} K^{-1})
h_m	membrane heat transfer coefficient (W m^{-2} K^{-1})
H_v	water vapor enthalpy (J mol^{-1})
i	subscript to indicate either feed solution (f) or distillate solution (d)
j	subscript to indicate either calcium (Ca^{2+}) or sulfate (SO_4^{2-})
J	water flux (L m^{-2} h^{-1} or mol m^{-2} s^{-1})
k_B	Boltzmann's constant (1.38×10^{-23} J K^{-1})
k_j	mass transfer coefficient of species j (m s^{-1})
Δm	mass of distillate water over time Δt (g)
n	number of molecules within a nucleating cluster
Nu_i	Nusselt number of solution i
Pr_i	Prandtl number of solution i
r	reaction rate constant (s^{-1})
R	gas constant (J mol^{-1} K^{-1})
R^*	critical recovery (m^3 m^{-3})
Re_i	Reynolds number of solution i
Δt	time interval (s)
$T_{d,\,b}$	bulk distillate solution temperature (°C or K)
$T_{d,\,m}$	interfacial distillate solution temperature (°C or K)
$T_{f,\,b}$	bulk feed solution temperature (°C or K)
$T_{f,\,m}$	interfacial feed solution temperature (°C or K)
V^*	critical recovery volume (m^3)
V_0	initial feed solution volume (m^3)
v_i	cross-flow velocity of solution i (m s^{-1})

Greek letters

α	surface energy of a nucleating cluster (J m^{-2})
γ_{ln}	interfacial energy between a liquid solution and crystal nucleus (J m^{-2})
δ_m	membrane thickness (m)
ε	membrane porosity (m^3 m^{-3})
η_i	viscosity of solution i (g m^{-1} s^{-1})
θ	intrinsic contact angle (degree or radius)
κ_i	thermal conductivity of solution i (W m^{-1} K^{-1})
κ_g	thermal conductivity of air (W m^{-1} K^{-1})
κ_m	thermal conductivity of the membrane (W m^{-1} K^{-1})
$\Delta\mu$	chemical potential difference of solute in the dissolved and crystal phase (J mol^{-1})
μ_{solute}	chemical potential of solute in the dissolved phase (J mol^{-1})
$\mu_{crystal}$	chemical potential of solute in the crystal phase (J mol^{-1})
ρ_i	density of solution i (g m^{-3})
σ	saturation index
Ω	crystal volume (m^3)

will further elevate its implementation in a broad variety of applications [4–7].

In MD, sparingly soluble mineral salts in the feed solution can rise above their saturation limits when high water recovery is achieved [8,9]. As a consequence, mineral scaling can occur due to direct nucleation onto the membrane surface and the accompanying crystal growth [10]. Mineral scaling may also occur via deposition of crystals that form in the bulk solution of the MD feed channel (i.e. homogeneous nucleation). However, studies have shown that homogeneous nucleation is not common and only dominates at extremely high concentrations [11,12]. Membrane scaling can lead to a reduction in membrane permeability due to pore blockage by the growing crystals. Interestingly, mineral scaling can also cause membrane wetting and subsequent contamination of the recovered volume of pure water upon pore wetting [13–15].

The typical methods of scaling mitigation in MD desalination include pretreatment via the addition of antiscalants into the MD feed solution to disrupt mineral salt nucleation and crystal growth [16,17], and chemical membrane cleaning using acids or chemicals with strong chelating ability [18,19]. Antiscalant addition works to delay scaling via either the chelating effect [20], where highly soluble molecules are formed in coordination with the target scalants, or via the direct

interruption of scalant nucleation by a ligand-exchange mechanism or long-range interaction between the charged nuclei surface and the antiscalant [21]. Other scaling mitigation methods attempted include the reduction in feed solution residence time by increasing crossflow rate, intermittent flux reversal, back-purging with air, and the tailoring of membrane surface properties such as roughness, hydrophobicity, and charge [22–32]. Notably, the use of superhydrophobic membranes with operational strategies to minimize scalant growth into pores appears to be a highly effective strategy for mitigating mineral scaling [23,33]. The development of improved scaling mitigation strategies relies on the fundamental understanding of the effects that operating parameters have on the propensity for scale formation [34–36].

Calcium and sulfate ions are abundant in natural water. Therefore, calcium sulfate dihydrate ($CaSO_4 \cdot 2H_2O$, gypsum), which is sparingly soluble, is one of the most commonly encountered scale-forming compounds in membrane processes for the treatment of high-salinity natural water such as seawater and brackish water [37–39]. The thermodynamic equilibrium of crystal nucleation from solution can be an informative metric for understanding the state of the bulk solution at the point when crystal growth is observed. It is theoretically expected that the thermodynamic state of a crystal-forming solution is independent of the operational parameters implemented during the crystallization

process. However, to date, no studies exist which systematically compare the thermodynamic state of the crystal-forming solution at the crystallizing interface across varying operational parameters (i.e., solution temperature and water flux).

Studies have suggested that gypsum scaling propensity in membrane desalination can be influenced by feed solution temperature and water flux [40,41]. Specifically, gypsum scaling induction is delayed when the feed solution temperature and the flux are simultaneously reduced [42]. In direct-contact MD (DCMD), mass transfer is driven by a vapor pressure gradient imposed between two solutions separated by a microporous, hydrophobic membrane [1,43,44]. The temperature-induced vapor pressure gradient is created by heating the feed solution contacting the hydrophobic membrane. Water evaporates at the membrane-feed interface, diffuses through the membrane pores, and condenses at the cooler membrane-distillate interface (Fig. 1). Because the water flux across the membrane is inherently linked to the temperature difference across the membrane, the isolation of one parameter is necessary to analyze the effects of the other parameter on mineral scaling.

In this study, the thermodynamic condition of the gypsum-forming solution at the feed-membrane interface is evaluated across varying operational conditions to assess the applicability of a thermodynamic model in predicting the behavior of gypsum scaling in MD. To facilitate the controlled variation of thermodynamic state at the crystallizing interface, the crystal precursor concentration and solution temperature are individually managed by conducting two series of MD experiments to isolate the independent effects of water flux and feed temperature. Then, the critical water recovery at the point of flux decline (i.e., the induction point) is compared to assess the variations in the estimated thermodynamic state and the sensitivity of the induction point to either operating parameter. The influence of both temperature polarization (TP) and concentration polarization (CP) are considered using established mass and heat transfer theory. The thermodynamic stability of the system is quantified using interfacial saturation index which is used to calculate the interfacial Gibbs free energy for nucleation.
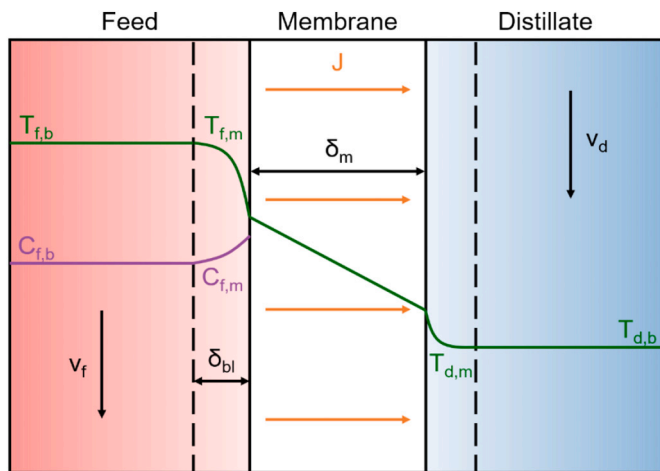
2. Theory and methodology

2.1. Temperature and concentration polarization in MD

To describe the interfacial conditions for gypsum nucleation on the MD membrane surface and therefore yield meaningful comparisons between scaling events across different MD experiments, it is necessary to evaluate TP and CP within the coupon-scale MD test cell. TP is a phenomenon in which the temperature of the feed solution tends to be lower at the feed-membrane interface than in the bulk solution, and, correspondingly, the temperature of the distillate tends to be higher at the membrane interface than in the bulk solution. TP is affected by both the conductive heat transferred between the feed solution and the membrane and the convective heat transferred due to the transport of water vapor across the membrane. Based on the method developed in previous work [45], which considers the flow of both of these convective and conductive heat transfer using a resistive framework, an overall heat balance was used to implicitly evaluate the interfacial temperatures in each experimental trial (Eq. (1)):

$$h_f\left(T_{f,b} - T_{f,m}\right) = JH_v + h_m\left(T_{f,m} - T_{d,m}\right) = h_d\left(T_{d,m} - T_{d,b}\right) \qquad (1)$$

where h_f, h_m, h_d are the heat transfer coefficients in the feed solution, membrane, and distillate solution, respectively; $T_{f,\,b}$ is the bulk feed solution temperature, $T_{f,\,m}$ is the interfacial feed solution temperature (at the feed/membrane interface), $T_{d,\,b}$ is the bulk distillate solution temperature, $T_{d,\,m}$ is the interfacial distillate solution temperature (at the distillate/membrane interface), J is the water vapor flux, and H_v is the enthalpy of water vapor.

The use of this heat balance to assess average interfacial properties on the module scale assumes (1) negligible heat losses into the surroundings, (2) a linear relationship between the mass water flux and the vapor pressure difference across the membrane, and (3) constant H_v despite small temperature changes along the length of the module. Several works have successfully applied a similar framework support experimental findings [46,47]. The Nusselt number was used to estimate h_f and h_d (Eq. (2)):

$$h_i = \frac{Nu_i \kappa_i}{d} \qquad (2)$$

where h_i is the heat transfer coefficient of solution i (either feed solution, in which case "i" is "f", or distillate, in which case "i" is "d"), Nu_i is the Nusselt number of the stream of solution i, κ_i is the thermal conductivity of solution i, and d is the hydraulic diameter of the flow channel. The thermal conductivities of the hydrophobic membrane polymer and of the air trapped within the membrane's pores were used to calculate h_m (Eq. (3)):

$$h_m = \frac{\kappa_g \varepsilon + \kappa_m(1-\varepsilon)}{\delta_m} \qquad (3)$$

where κ_g is the thermal conductivity of air, κ_m is the thermal conductivity of the membrane, ε is the porosity of the membrane, and δ_m is the membrane thickness. The established correlation between the Nusselt number, the Reynolds number, and the Prandtl number was used to calculate Nu_i (Eq. (4)):

$$Nu_i = a_i Re_i^{b_i} Pr_i^{c_i} \qquad (4)$$

where Re_i is the Reynolds number of solution i, Pr_i is the Prandtl number of solution i, and a_i, b_i, and c_i are the Nusselt coefficients of solution i. While c_i is usually assigned the value of $1/3$ in MD literature [48–50], the other Nusselt coefficients (a_i and b_i) were determined iteratively by constraining them within the range that would yield a value for Nu_i within the same flow regime (i.e., turbulent or laminar) identified through calculation of Re_i. The known physical properties of the solutions and of the flow channel were used to calculate Re_i and Pr_i (Eqs. (5)

Fig. 1. Schematic of the membrane distillation (MD) process, including bulk feed temperature ($T_{f,\,b}$), interfacial feed temperature ($T_{f,\,m}$), bulk feed concentration ($c_{f,\,b}$), interfacial feed concentration ($c_{f,\,m}$), feed solution velocity (v_f), feed boundary layer for mass transfer (δ_{bl}), water flux (J), MD membrane thickness (δ_m), bulk distillate temperature ($T_{d,\,b}$), interfacial distillate temperature ($T_{d,\,m}$), and distillate solution velocity (v_d). The profile of salt concentration in the distillate is not shown because the distillate contains no salt in a functional MD membrane with a salt rejection close to 100%. (For interpretation of the references to colour in this figure, the reader is referred to the web version of this article.)

and (6)):

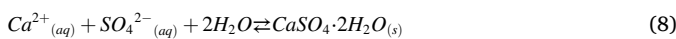$$Re_i = \frac{v_i d \rho_i}{\eta_i} \qquad (5)$$

$$Pr_i = \frac{\eta_i C_{p,i}}{\kappa_i} \qquad (6)$$

where v_i is the cross-flow velocity of solution i, ρ_i is the density of solution i, η_i is the viscosity of solution i, and $C_{p,i}$ is the specific heat capacity of solution i.

Concentration polarization (CP) is the phenomenon in membrane-based separation where the solute concentration is higher at the membrane interface when compared to the bulk solution. CP is driven by the convective water flow from the bulk solution toward the membrane surface. As water continuously evaporates at the feed/membrane interface, solutes remain at the interface and a gradient in solute concentration across the mass transfer boundary layer is established (Fig. 1, purple curve). CP can be calculated using (Eq. (7)) [51].

$$C_{m,j} = C_b exp\left(\frac{J}{k_j}\right) \qquad (7)$$

where $C_{m,j}$ is the concentration of species j at the feed-membrane interface, C_b is the bulk solute concentration, and k_j is the mass transfer coefficient of species j. The molecular diffusivity of the sulfate ion (SO_4^{2-}) is greater than that of the calcium ion (Ca^{2+}), and k_j is dependent on ion diffusivity and the hydrodynamic condition of the feed/membrane interface. Therefore, a solution with an identical C_b of Ca^{2+} and SO_4^{2-} will result in a C_m of SO_4^{2-} which is less than that of Ca^{2+}. The stoichiometry of gypsum formation (Eq. (8)) dictates that the molar ratio of the precipitating Ca^{2+} and SO_4^{2-} to be 1:1. The limiting reactant for gypsum formation is the species which is present in the lower concentration. To reflect this assumption that the amount of gypsum formed within the solution can be no greater than the amount of the limiting reactant, the C_m of SO_4^{2-} is used to represent the interfacial solute concentration in this work. However, the partial vapor pressure calculated at the feed-membrane interface (via Antoine's equation) considered the concentration of both Ca^{2+} and SO_4^{2-}.

$$Ca^{2+}{}_{(aq)} + SO_4{}^{2-}{}_{(aq)} + 2H_2O \rightleftarrows CaSO_4 \cdot 2H_2O_{(s)} \qquad (8)$$

2.2. Gypsum nucleation and growth

Gypsum nucleation and growth can be assumed to follow the principles described in classical nucleation [52]. The equilibrium chemical potential of the crystal-forming ions within an aqueous solution can be described as the difference between the solute chemical potential and the chemical potential of the same species in the solid crystal phase (Eq. (9)) [53].

$$\Delta\mu = \mu_{solute} - \mu_{crystal} \qquad (9)$$

where $\Delta\mu$ is the chemical potential difference between the two phases within the system, μ_{solute} is the chemical potential of the solute, and $\mu_{crystal}$ is the chemical potential of the crystal. When the solute chemical potential is greater than the chemical potential of the same species in crystal, the solution is supersaturated. Given sufficient time, this supersaturated solution will eventually approach equilibrium through the formation of crystal via precipitation reaction, which lowers the chemical potential of the solutes and tends to reduce the system free energy. The chemical potential difference is often quantified using the saturation index (σ, or SI) defined as the following:

$$\sigma = ln\left(\frac{IAP}{K_{sp}}\right) = \frac{\Delta\mu}{k_B T} \qquad (10)$$

where IAP is the ion activity product of the crystal-forming ions, K_{sp} is

the solubility product of the precipitate, and $k_B T$ is the thermal energy.

At the same time, the formation of nuclei creates new solid/water interface, which tends to increase the system free energy. Together, these competing effects of free energy loss (due to phase change) and gain (due to increased surface area) contribute to a free energy profile as a function of the size of nucleating cluster (Eq. (11)) [54].

$$\Delta G(n) = -n\Delta\mu + A_S n^{2/3}\alpha(n) \qquad (11)$$

where $\Delta G(n)$ is the free energy change associated with the formation of clusters of n ion pairs within the supersaturated solution, $-n\Delta\mu$ is the decrease in chemical potential caused by the formation of clusters of n molecules, and $A_S n^{2/3}\alpha(n)$ is the free energy gain caused by the creation of a new interface with a surface area of A_S and an interfacial energy of $\alpha(n)$. The number of ion pairs within the cluster is considered because a supersaturation condition alone is insufficient to induce precipitation with finite kinetics.

Before crystals begin to develop, the solution must produce or contact nuclei or seeds which act as centers for crystallization. If too few ion pairs are present within a nascent cluster, growing such a cluster increases the system free energy due to the creation of interfaces and is thus energetically unfavorable. Consequently, the newly formed cluster is likely to dissolve back into solution [55]. Therefore, a critical cluster size exists beyond which the continued decrease in chemical potential results in crystal growth rather than crystal dissolution. This phenomenon is referred to as the Gibbs-Thomson effect, and leads to the understanding of the existence of the critical nucleus size for crystal formation (Fig. 2A) [56]. The critical size with a spherical particle assumption (although questionable) can be evaluated by finding the maximum of $\Delta G(n)$ based on Eq. (11). The energy barrier for homogeneous nucleation can then be expressed as

$$\Delta G^*_{hom} = \frac{16\pi\gamma_{ln}^3 \Omega^2}{3(k_B T\sigma)^2} \qquad (12)$$

where γ_{ln} is the interfacial energy between the liquid solution and the crystal nucleus, Ω is the volume of a crystal unit (i.e., molar volume divided by Avogadro's number),

The critical nucleus size and the energy barrier of nucleation are important to consider for membrane scaling, because only the nuclei that have assembled beyond this limit will contribute to scale growth. According to such a theory, a metastable state exists where the solution contains a concentration of crystal-forming ions beyond the solubility limit of the associated crystal, but the nuclei have not formed and oriented into a fixed lattice exceeding the critical size from which successive growth can continue [57].

Traditionally, nucleation theory distinguishes between homogeneous nucleation and heterogeneous nucleation. Homogeneous nucleation refers to the formation of nuclei in the absence of foreign particles or surfaces within the initial single phase, while heterogeneous nucleation refers to nucleation induced by surfaces that are different from the crystallizing substance [59]. It is generally accepted that nucleation onto foreign particles or surfaces is more kinetically favorable than homogeneous nucleation [60]. The metastable zone (Fig. 2B), which arises from the constant formation and dissolution of nuclei, can be manipulated by adding particles to the solution or by otherwise increasing the probability of the generation of nuclei which are above the critical size [54]. While crystal formation in solution (i.e., homogeneous nucleation) can be controlled in this way, crystal nucleation can also be controlled by adjusting the surface energy of the nucleating surface during heterogeneous nucleation [61,62]. The energy barrier for heterogeneous nucleation, ΔG_{het}^*, can be obtained by modifying Eq. (12) with a correction factor that accounts for the interaction between the crystal and the surface it grows on [63–66]:

$$\Delta G_{het}^* = \frac{16\pi\gamma_{ln}^3 \Omega^2}{3(k_B T\sigma)^2}\left[\frac{1}{4}(1 - cos\theta)^2(2 + cos\theta)\right] \qquad (13)$$
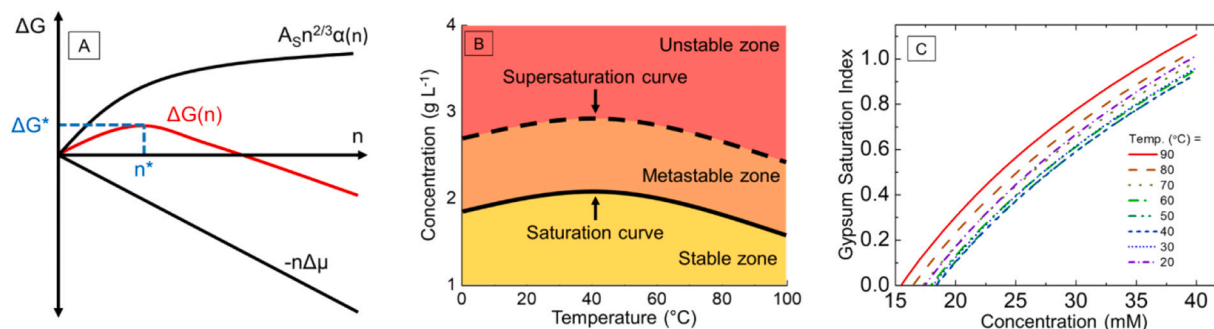
Fig. 2. (A) Illustration of the components of the work of nucleation and the resulting basis for the critical free energy barrier for crystal formation (ΔG^*) and the associated critical nucleus cluster size (n^*). As new clusters form within a saturated solution, the total change in free energy is both decreased due to a reduction of chemical potential within the solution ($-n\Delta\mu$) and increased due to the formation of new favorable surfaces from which to nucleate ($A_s n^{2/3}\alpha(n)$). When the number of molecules within a crystal cluster is equal to n^*, the work of nucleation is maximized (ΔG^*) and successive crystal growth lowers the free energy of the system. (B) Ostwald-Miers diagram showing the stable, metastable, and unstable zones of solubility for calcium sulfate dihydrate (gypsum) from 0 to 100 °C [58]. The solid curve represents the saturation limit of gypsum at each temperature, and the dashed line represents the supersaturation limit of gypsum at each temperature. (C) Theoretical gypsum saturation index as a function of solution temperature and equimolar Ca^{2+} and SO_4^{2-} concentration. In accordance with gypsum solubility data, the saturation index is at a minimum near 40 °C which is near gypsum's maximum solubility.

where θ is the intrinsic contact angle between a nucleus (of a hypothetical shape of a spherical cap) and the substrate it adheres to, when both are submerged in solution. We note that θ is a fictitious parameter as crystals do not form a sessile drop of a spherical cap geometry on a submerged solid substrate. Rather, θ is a hypothetic parameter that quantifies the interaction between the nucleus and the substrate in water, following the Young-Dupre equation, $\cos\theta = (\gamma_{sw} - \gamma_{sc})/\gamma_{cw}$, where γ_{sw}, γ_{sc} and γ_{cw} stand for the interfacial energy between substrate and water, between substrate and crystal, and between crystal and water, respectively. From the limited studies performed in this area, it appears $\Delta G_{het}^*/\Delta G_{hom}^*$, which equals $(1 - \cos\theta)^2(2 + \cos\theta)/4$, was experimentally determined [67,68]. Alternatively, θ may also be determined from the extended Young-Dupré equation considering the both the Liftshitz-van der Waals interaction and the polar interaction [69]. These interaction parameters may be determined from the measured liquid sessile drop contact angles on both the substrate and on the crystal.

The solubility product constant for gypsum as a function of temperature has been obtained by Marshall and Slusher [70] and others [71,72] for solutions from 0 to 100 °C, which informs the inverted solubility-temperature relationship above ~40 °C (Fig. 2B). Both solute concentration and temperature affect the saturation index (Fig. 2C), as the solute concentration determines the *IAP* and temperature influences the K_{sp}. Both parameters also affect the energy barrier (Eqs. (12) and (13)) through σ, but temperature also exerts an extra (and strong) impact through the square of $k_B T$ in the denominator.

2.3. Membrane distillation experiments

2.3.1. Salts and membranes

Calcium chloride ($CaCl_2$) and sodium sulfate (Na_2SO_4) were purchased from Research Products International (Mount Prospect, IL). Both salts were used as received without further purification. Poly vinylidene fluoride (PVDF) membranes with a nominal pore diameter of 0.45 μm were purchased from GE Healthcare (Chicago, IL).

2.3.2. Experimental setup for membrane distillation

A custom-made DCMD cell was used to perform the experiments in this study (Fig. S1). Centrifugal pumps were used to circulate the feed solution and the distillate through the DCMD unit on either side of the MD membrane. The feed and distillate temperatures were monitored using digital temperature probes at the entrance and exit of both streams and adjusted using digitally controlled constant-temperature baths (Fig. S2). The distillate conductivity was measured over time using a

conductivity probe. The water flux was monitored by calculating the mass of water transferred through the membrane using the time series of the distillate mass following Eq. (14):

$$J = \frac{\Delta m}{(\Delta t)\rho_d A_m} \tag{14}$$

where J is water flux, Δm is the mass of the distillate water collected over time (Δt), ρ_d is the density of the distillate water, and A_m is the active area of the membrane.

2.3.3. Membrane distillation scaling experiments

Each of the gypsum scaling experiments in this study were conducted using a 1 L feed solution composed of 20 mM $CaCl_2$ and 20 mM Na_2SO_4. The flowrates used for the feed solutions and distillate were 0.3 and 0.2 L min^{-1}, respectively. Based on the geometry of the custom-built membrane testing cell, the crossflow velocity calculated for the feed and distillate solutions was 0.08 and 0.05 m s^{-1}, respectively. Prior to the commencement of each experiment, the temperatures of each stream and the water flux through the membrane were stabilized for at least 2 h using deionized (DI) water as in both feed and distillate channels. $CaCl_2$ and Na_2SO_4 were added (5 min apart) in the hot feed reservoir once the hot and cool streams reached the target operating temperature and the target water flux was achieved. The feed reservoir containing the salt solutions was stirred continuously, and although the maximum solubility of gypsum is about 15.5 mM (at 40 °C), no suspended particles were observed before or during the experiments. This suggests that the initial feed solutions were metastable and remained in a metastable state before flux decline resulting from pore blockage was observed. The changes in both density and partial vapor pressure between DI water and the feed solutions were small (less than 2%) for each stream [73], so the average water flux measured during the stabilization period was not observed to change after $CaCl_2$ and Na_2SO_4 addition.

The values of critical recovery (R^*) in this study were taken to be the water recovery (in percentage) at the point when scaling reduced flux to 85% of its original value. This cutoff percentage is not meant to imply any theoretical significance (e.g., related to the critical nucleus size), but rather to give a consistent threshold for the identification of the induction point described in other works without direct observation of gypsum nucleation via feed solution conductivity or quartz crystal microbalance measurements [74,75]. The identity of the scale layer which formed on the membrane surfaces was characterized using X-ray powder diffraction (XRD). The values for critical gypsum-forming ion concentration (in the bulk solution) were calculated as the original bulk concentration multiplied by the volumetric concentration factor at the

critical recovery point (Eqs. (15) and (16)):

$$R^* = \frac{V^*}{V_0} \times 100\% \tag{15}$$

$$C_b^* = \frac{C_{b,0}}{1 - \frac{V^*}{V_0}} \tag{16}$$

where V^* is the critical recovery volume, V_0 is the initial feed solution volume, C_b^* is the critical ion concentration of the feed solution, and $C_{b,0}$ is the initial ion concentration of the feed solution.

2.4. Evaluation of the impact of feed temperature and water flux on gypsum scaling

Gypsum scaling during membrane processes is influenced by a number of factors, including the crystal-forming ion concentration (i.e. saturation level) and solution temperature. To investigate a collection of scenarios to compare gypsum scaling with varying saturation levels and solution temperatures at the membrane interface, two series of experiments were conducted (Fig. 3). The bulk feed temperature range in Series 1 (50.5 to 77.8 °C) and water flux range in Series 2 (11.4 to 38.9 L m^{-2} h^{-1}) were chosen because they are within the representative magnitude of the parameters that are used in pilot-scale MD applications [76–78].

2.4.1. MD experiments with constant flux and varied feed temperature (Series 1)

In the first series of experiments (Series 1), the bulk feed temperature was varied from 50.5 to 77.8 °C while the bulk distillate temperature was simultaneously increased (via trial-and-error) to maintain a constant vapor flux near 15 L m^{-2} h^{-1} (15.15 ± 0.34 L m^{-2} h^{-1}) (Fig. 3A and Table S1). This allowed for the independent evaluation of temperature effects on gypsum formation without influence from the effects of mismatched water flux. As the partial vapor pressure increases much more rapidly in the higher temperature range than in the lower temperature range according to Antoine equation, the temperature difference between the feed solution and distillate to maintain the same partial vapor pressure difference (for achieving the same flux) is substantially smaller in the higher temperature range (Table S1).

2.4.2. MD experiments with constant feed temperature and varied flux (Series 2)

In the second series of experiments (Series 2), the bulk feed temperature was maintained near 70 °C (70.93 ± 0.89 °C) while bulk distillate temperature was adjusted to achieve vapor fluxes ranging from 11.4 to 38.9 L m^{-2} h^{-1} (Fig. 3B and Table S1). Isolating the effects of water flux without changing the feed temperature allows for the direct evaluation of CP and TP on gypsum scaling in MD.

3. Results and discussion

3.1. Interfacial temperatures and ion concentration

To determine the effects of temperature and water flux on the mass and heat transfer across the membrane, the interfacial feed temperatures and ion concentrations were calculated for each series using Eq. (1) through Eq. (7) considering temperature and concentration polarizations. The simulated results (based on experimentally measurable parameters) show the dependence of interfacial feed temperature and ion concentration on the bulk temperature and water flux (Fig. S3). For Series 1 (constant flux), temperature polarization was more severe with a lower bulk feed temperature because the bulk temperature difference between the feed and the distillate was substantially larger at a lower bulk feed temperature (Fig. 3A). For Series 2 (constant bulk feed temperature at 70 °C), temperature polarization was expectably more significant at a higher flux (Fig. 4A, Fig. S4).

The initial interfacial ion concentrations in Series 1 (constant flux) were constant as the same flux resulted in the same degree of concentration polarization. The value of CPC was ~1.25 based on the vapor flux and the hydrodynamic conditions of boundary layer (Fig. S4). In Series 2 (constant feed temperature), the impact of varied water flux on interfacial concentration was consequential. As water flux increased from 10 to 40 L m^{-2} h^{-1}, interfacial ion concentration increased from 23 to 35 mM (Fig. S3).

3.2. Scaling behavior of gypsum at varying bulk feed temperature and water flux

A total of sixteen different scaling experiments were performed to compare the conditions at the feed-membrane interface at the point when gypsum scale begins to reduce mass transfer during direct-contact MD. The individual impacts of bulk feed solution temperature and water flux on pure water recovery and gypsum saturation index at the point of flux decline were assessed. In each trial, the initial feed solution was composed of 20 mM CaCl$_2$ and 20 mM Na$_2$SO$_4$. As water was recovered, the feed solution became increasingly concentrated and supersaturated. Significant flux decline was observed in each trial as gypsum crystals
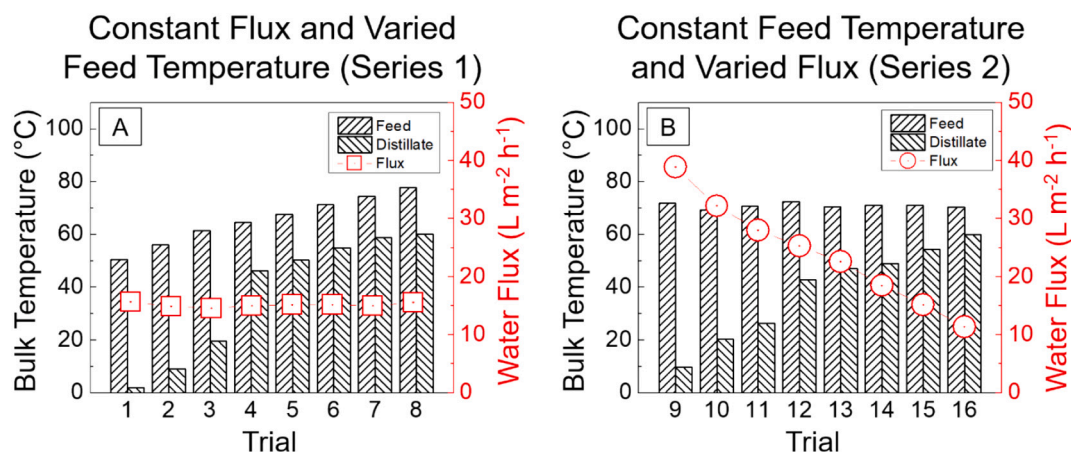

Fig. 3. Solution temperatures and water fluxes for varying gypsum scaling membrane distillation trials with (A) constant water flux, varied bulk feed solution temperature and (B) constant bulk feed solution temperature, varied water flux. In Series 1, the interfacial thermodynamic environment observed upon scaling was compared across varying temperatures, with all other operating parameters held constant. In Series 2, the interfacial thermodynamic environment was altered in both temperature and ion concentration because of the varied flux.
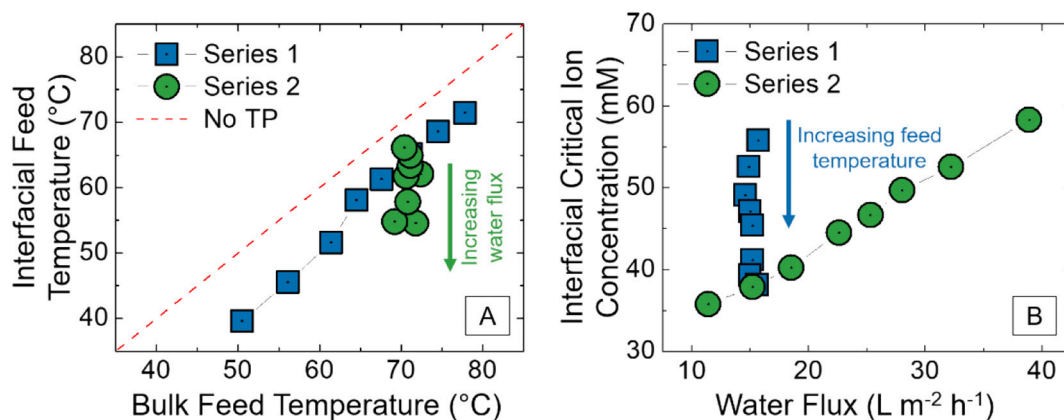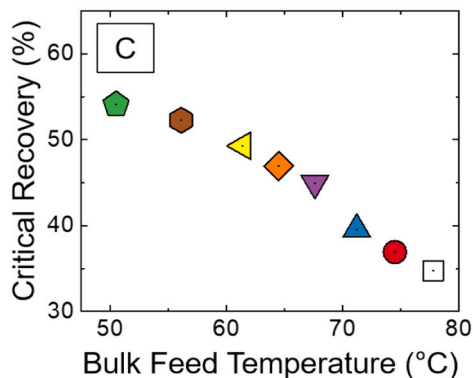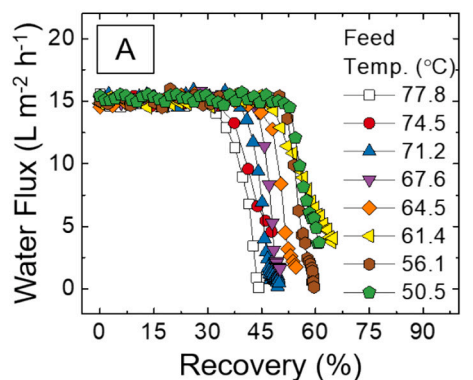
Fig. 4. (A) Interfacial feed temperature versus bulk feed temperature and (B) interfacial initial ion concentration versus water flux for constant flux Series 1 (blue squares) and constant bulk feed temperature Series 2 (green circles). The red dashed lines in panel (A) represents the expected interfacial temperature absent the influence of TP. TP results in interfacial feed solution temperatures below bulk feed solution temperatures. The magnitude of TP increases with increased feed-distillate temperature difference for Series 1 and with increased water flux for Series 2. (For interpretation of the references to colour in this figure legend, the reader is referred to the web version of this article.)

formed and grew to cover the membrane pores [79]. The observation that gypsum was the only precipitating phase of calcium sulfate within the temperature range explored, as opposed to simultaneous or competitive precipitation of calcium sulfate anhydrite ($CaSO_4$) and calcium sulfate hemihydrate ($CaSO_4 \cdot 1/2H_2O$, bassanite), is confirmed by XRD analysis (Fig. S5) and is in agreement with results from previous studies [74,80].

The critical recovery (as marked by flux decline to 85% of initial flux) achieved during each scaling experiment ranged from 30 to 60% for Series 1 with varied bulk feed temperature (Fig. 5A, C) and from 30 to 40% for Series 2 with varied flux (Fig. 5B, D). With a constant water flux (Series 1), a higher bulk feed temperature resulted in earlier flux decline
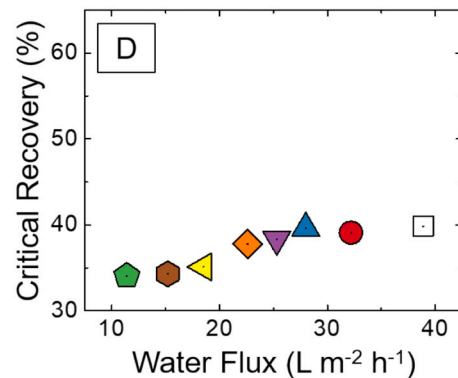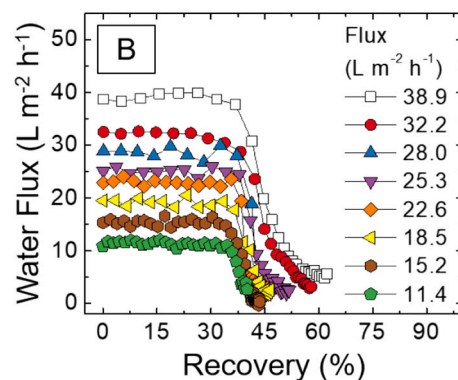

Fig. 5. Results from 16 experimental trials where (A, C) water flux was held constant with varied bulk feed solution temperature, and (B, D) bulk feed solution temperature was held constant with varied water flux. (A, B) Water flux versus pure water recovery, and critical recovery versus (C) bulk feed temperature and (D) water flux. Each MD trial was executed using an initial feed composition of 20 mM Ca^{2+} and 20 mM SO_4^{2-}. The bulk solution temperatures varied according to (Table S1). The critical recovery (C, D) was taken to be the percentage of pure water recovered from the feed solution into the distillate solution at the point where the flux was reduced to 85% of its original average value.

and thus a lower critical recovery (Fig. 5C). With a constant feed temperature (Series 2), a higher flux led to a higher critical recovery, but the dependence of critical recovery on flux was relatively small as compared to that on feed temperature (Fig. 5D). We note that even with a constant bulk feed temperature (as in Series 2), the interfacial temperature decreased with increasing vapor flux (Fig. 4A). Therefore, the slightly higher critical recovery observed with a higher water flux in Fig. 5D may also result from a reduction of interfacial temperature in addition to the higher interfacial ion concentration due to stronger concentration polarization.

3.3. Thermodynamic conditions at the interface upon scaling

To facilitate further analysis, we define the saturation index at the critical recovery point as the "critical SI". The critical SI in the bulk and near the membrane interface are termed as "bulk critical SI" and "interfacial critical SI", respectively. The interfacial critical SI quantifies the deviation of interfacial thermodynamic condition from the thermodynamic equilibrium of gypsum formation at the critical recovery. In theory, several factors affect the interfacial critical SI, including critical recovery, flux, and interfacial temperature (note that critical recovery and the interfacial critical SI are interdependent). Higher flux and critical recovery both contribute to higher interfacial ion activity product, thereby increasing the critical SI. As the interfacial feed temperature was almost always higher than 40 °C (Fig. 4A), a higher interfacial temperature (given other parameters maintained constant) would tend to increase the critical SI by slightly reducing the solubility (Fig. 3B). However, this does not mean that the critical SI will in fact increase with increasing interfacial temperature as the interfacial temperature also has impacts on flux and critical recovery.

The analysis of experimental data from both series of experiments suggests that the interfacial critical SI negatively correlates with the interfacial feed temperature, regardless of whether higher interfacial temperature was achieved by increasing the feed temperature or reducing the vapor flux (Fig. 6A). The interfacial critical SI is also quasilinear to the interfacial critical ion concentration (Fig. 6B). This second correlation can be readily explained based on the definition of saturation index (Eq. (10)) and the relatively weak dependence of K_{sp} on temperature, and is thus not as informative as the correlation with temperature.

The negative correlation between interfacial temperature and the interfacial critical SI suggests that the solution can sustain a higher degree of oversaturation at a lower interfacial temperature. The concept of interfacial critical SI captures the impacts of interfacial temperature and ion concentration on the deviation of the interfacial solution from

precipitation equilibrium. Therefore, if the scaling process were to be controlled solely by thermodynamics, it would be reasonable to hypothesize that all experiments would yield a similar interfacial critical SI regardless of the experimental conditions. This is equivalent to stating that, regardless of the interfacial temperature and ion concentrations, scaling occurs at a similar degree of oversaturation. However, such a constant interfacial critical SI has not been observed throughout different experimental conditions. The lack of such a constant interfacial critical SI and the universally observed strong dependence of interfacial critical SI on interfacial temperature both suggest that kinetics of precipitation plays an important role in gypsum scaling. These results are consistent with other studies that build upon the generally accepted theory of gypsum precipitation kinetics and thermodynamics [81,82], in that higher temperatures accelerate nucleation kinetics.

3.4. Energy barrier of nucleation and scaling mode

The consideration of kinetics can be facilitated using the activation energy barrier (ΔG^*) in the free energy curve for reaction which describes the free energy of the system as a function of the reaction process. In the case of nucleation, the reaction process is described by the nucleus radius. If we can increase the interfacial temperature without changing the interfacial ion concentration, the temperature increase should have two major effects on the shape of the energy curve. First, a higher temperature should increase the Gibbs free energy of nucleation and the saturation index, as Gibbs free energy is proportional to $k_B T$ and K_{sp} is negatively dependent on temperature in the studied temperature range. However, these impacts only concern thermodynamics that quantifies the deviation of the solution at the interface from its ion-mineral equilibrium condition.

The second impact of temperature, which is perhaps more important, is the enhanced kinetics at higher temperature due to both reduced activation energy barrier (ΔG^*) as predicted by Eqs. (12) and (13) (depending on nucleation mode) and the increased thermal energy of ions. Eqs. (12) and (13) suggest that ΔG^* is inversely proportional to the square of the product of temperature and SI. For example, by increasing the temperature from 40 °C (~313 K) to 70 °C (~343 K), ΔG^* decreases by more than ~20% while the thermal energy ($k_B T$) increases by ~10%, both promoting the nucleus to grow beyond the critical nucleus size (i.e., to overcome the energy barrier).

Ion concentration also affects the energy barrier of nucleation according to Eqs. (12) and (13). Specifically, ΔG^* is inversely proportional to the square of SI. Thus , increasing the ion concentration alone tends to reduce ΔG^*. In the Series 2 experiments (constant bulk feed
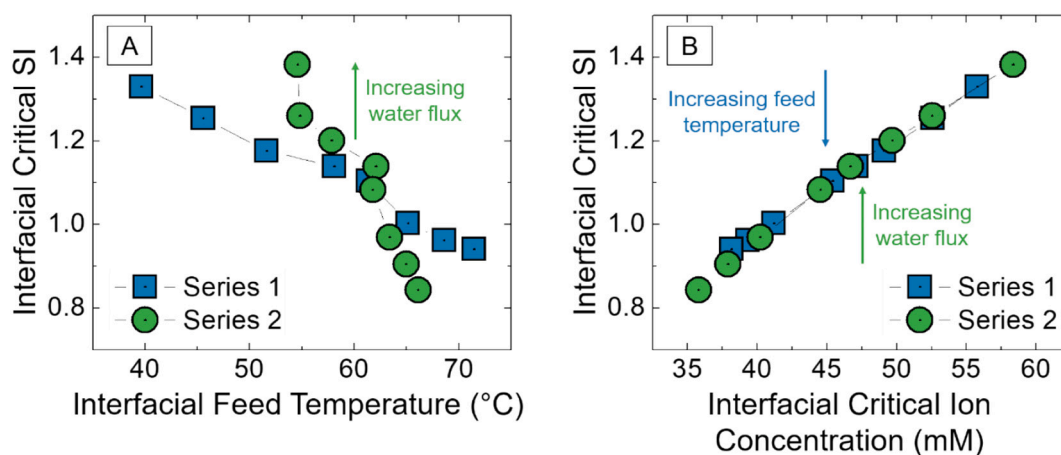

Fig. 6. Interfacial critical saturation index versus (A) interfacial feed temperature and (B) interfacial critical ion concentration for the constant flux with varied bulk feed temperature Series 1 (blue squares) and the constant bulk feed temperature with varied water flux Series 2 (green circles). The interfacial critical saturation index was calculated using the interfacial ion concentration estimated from the volume remaining in the feed solution when the water flux fell below 85% of its initial value. (For interpretation of the references to colour in this figure legend, the reader is referred to the web version of this article.)

temperature), however, a higher flux did not only result in a higher initial interfacial ion concentration but also reduced the interfacial temperature due to stronger temperature polarization. Therefore, the impact of increased interfacial SI at higher flux on ΔG^* was to a certain extent offset by the reduced interfacial temperature.

To evaluate the activation energy barrier using Eqs. (12) or (13), we need the values of several parameters, including the unit volume of the crystal (Ω: 0.496 nm^3) [59], the interfacial energy between water and the nucleus (γ_{ln}), and in the case of heterogenous nucleation, the contact angle between the crystal and the substrate membrane when both are submerged in water (θ). Accurate evaluation of γ_{ln} and θ is not trivial. In this study, we use a θ of 57.5° as reported in literature [83], noting that the correction factor $(1 - \cos(\theta))^2(1 + \cos(\theta))/4$ in Eq. (13) always ranges from zero to one. The choice of γ_{ln} is tricky as the literature reports values that span over an order of magnitude (from 4 to 100 mJ m^{-2}) [84] and the activation energy barrier is highly sensitive to γ_{ln} ($\Delta G^* \propto \gamma_{ln}^3$). We decide to choose the lowest value (4 mJ m^{-2}), because larger values of γ_{ln} will result in activation energy barrier (even for heterogeneous nucleation) that is too large (as compared to thermal energy) for any nucleation to occur.

We evaluate three activation energy barriers at the critical recovery, including that for homogenous nucleation in the bulk solution, homogeneous nucleation in the solution phase near the membrane surface, and heterogeneous nucleation at the feed/membrane interface (Table S2). Eqs. (12) and (13) are used to calculate ΔG^* for homogeneous nucleation and heterogeneous nucleation, respectively, along with the solution conditions (i.e., temperature and ion concentration) relevant to the respective location of nucleation. Specifically, the experimentally measured critical recovery allows the determination of the bulk ion concentration, whereas the interfacial temperature and ion concentration were determined using well-established mass and heat transfer model as detailed in Section 2.1. We compare these energy barriers to the thermal energy k_BT as the reference energy level. However, we recognize that the precipitation process differs from other phenomena such as chemical reaction or colloidal interaction, where the energy curve describes the event of a single "particle", the energy curve in precipitation describes the collective event of a group of "particles".

From such calculations, we observe that the energy barrier of homogeneous nucleation, whether it is in the bulk or near the membrane surface, was significantly higher than thermal energy of ions in the respective positions when critical recovery was reached (Fig. 7). This suggests that formation of gypsum precipitates in the solution phase along with deposition of such precipitates onto the membrane surface was unlikely the primary mechanism of scaling. In contrast, heterogeneous nucleation onto the membrane surface only required an activation energy barrier that was lower than the thermal energy. The low activation energy barrier for heterogeneous nucleation stems mainly from the fact that the correction $(1 - \cos\theta)^2(2 + \cos\theta)/4$ with a θ of 57.5° has a value of ~0.134, which substantially reduces the energy barrier and its dependence on temperature and flux (as compared to homogeneous nucleation).

These observations, which were consistent in both series of experiments (constant flux vs. constant feed temperature), suggest heterogeneous nucleation should be the dominant mechanism for scaling. Such a prediction is consistent with our experimental observations (in this study) that the feed solution remained clear, i.e., no homogeneous nucleation was observed, at the critical recovery or at any point during the trials. However, we recognize the limitation of the above analysis for the lack of consideration of the local hydrodynamic condition. While previous studies have shown the significant impacts of flow conditions on the scaling induction, it was unclear if the hydrodynamic conditions affect scaling directly, which is not considered under the current framework, or indirectly via their impacts on the spatial distributions of temperature and ion concentrations.

4. Conclusion

In this work, we examine the correlations between the behavior of gypsum scaling in MD and the thermodynamic conditions of the feed solution. Specifically, we focused on the metric of critical recovery, i.e., the water recovery at which substantial flux decline (15%) is observed, to evaluate the impacts of the feed temperature and vapor flux. By performing systematic experiments to control either the (bulk) feed temperature or the flux, we found that the critical recovery is more strongly dependent on feed temperature and less dependent on vapor flux. We also found that gypsum scaling is largely kinetically controlled
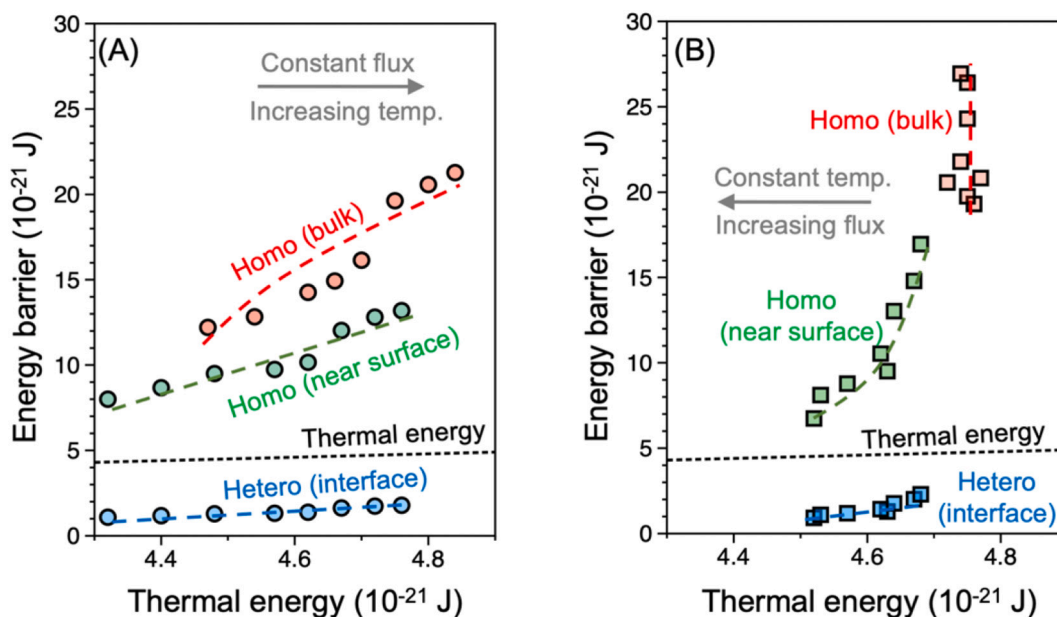

Fig. 7. Activation energy barriers vs. thermal energy for different nucleation modes at critical recovery for (A) Series 1 experiments with constant flux, and (B) Series 2 experiments with constant feed bulk temperature. Red: homogeneous nucleation in the bulk; Green: homogeneous nucleation near the membrane surface; Blue: heterogeneous nucleation. The thermal energy is also given as the dashed line. Points on the dash line have activation energy barrier being equal to thermal energy. (For interpretation of the references to colour in this figure legend, the reader is referred to the web version of this article.)

based on the lack of a condition-independent interfacial critical saturation index, and that temperature has a strong effect on the kinetics via both influencing the activation energy barrier of nucleation and the thermal energy. By carefully analyzing the bulk and interfacial conditions at the critical recovery, we also identified interfacial crystallization onto the membrane surface as the most probable mechanism of gypsum scaling in this study, which is consistent with experimental observation of lack of gypsum precipitation in the bulk.

CRediT authorship contribution statement

Kofi Christie: data collection and analysis, data curation and visualization, writing - original draft preparation.
Thomas Horseman: data collection and analysis, writing - original draft preparation.
Ruoyu Wang: analysis, modeling.
Chunlei Su: data collection and analysis.
Tiezheng Tong: analysis, writing - reviewing and editing.
Shihong Lin: conceptualization, analysis, writing - reviewing and editing.

Declaration of competing interest

The authors declare that they have no known competing financial interests or personal relationships that could have appeared to influence the work reported in this paper.

Acknowledgments

Appendix A. Supplementary data

Supplementary data to this article can be found online at https://doi.org/10.1016/j.desal.2021.115499.

References

[1] A. Alkhudhiri, N. Darwish, N. Hilal, Membrane distillation: a comprehensive review, Desalination 287 (2012) 2–18, https://doi.org/10.1016/j.desal.2011.08.027.

[2] A. Deshmukh, C. Boo, V. Karanikola, S. Lin, A.P. Straub, T. Tong, D.M. Warsinger, M. Elimelech, Membrane distillation at the water-energy nexus: limits, opportunities, and challenges, Energy Environ. Sci. 11 (5) (2018) 1177–1196, https://doi.org/10.1039/c8ee00291f.

[3] A. Liponi, C. Wieland, A. Baccioli, Multi-effect distillation plants for small-scale seawater desalination: thermodynamic and economic improvement, Energy Convers. Manag. 2020 (November 2019) 205, https://doi.org/10.1016/j.enconman.2019.112337.

[4] K.S.S. Christie, T. Horseman, S. Lin, Energy efficiency of membrane distillation: simplified analysis, heat recovery, and the use of waste-heat, Environ. Int. 2020 (138) (November 2019), 105588, https://doi.org/10.1016/j.envint.2020.105588.

[5] M. Tang, K.S.S. Christie, D. Hou, C. Ding, X. Jia, J. Wang, Fabrication of a novel underwater-superoleophobic/hydrophobic composite membrane for robust anti-oil-fouling membrane distillation by the facile breath figures templating method, J. Membr. Sci. 2021 (617) (August 2020), 118666, https://doi.org/10.1016/j.memsci.2020.118666.

[6] D. Hou, K.S.S. Christie, K. Wang, M. Tang, D. Wang, J. Wang, Biomimetic superhydrophobic membrane for membrane distillation with robust wetting and fouling resistance, J. Membr. Sci. 2020 (599) (November 2019), 117708, https://doi.org/10.1016/j.memsci.2019.117708.

[7] A. Deshmukh, M. Elimelech, Understanding the impact of membrane properties and transport phenomena on the energetic performance of membrane distillation desalination, J. Membr. Sci. 539 (March) (2017) 458–474, https://doi.org/10.1016/j.memsci.2017.05.017.

[8] D.M. Warsinger, J. Swaminathan, E. Guillen-Burrieza, H.A. Arafat, V.J.H. Lienhard, Scaling and fouling in membrane distillation for desalination applications: a review, Desalination 356 (2015) 294–313, https://doi.org/10.1016/j.desal.2014.06.031.

[9] K.S.S. Christie, Y. Yin, S. Lin, T. Tong, Distinct behaviors between gypsum and silica scaling in membrane distillation, Environ. Sci. Technol. 54 (1) (2020) 568–576, https://doi.org/10.1021/acs.est.9b06023.

[10] T. Tong, A.F. Wallace, S. Zhao, Z. Wang, Mineral scaling in membrane desalination: mechanisms, mitigation strategies, and feasibility of scaling-resistant membranes, J. Membr. Sci. 579 (February) (2019) 52–69, https://doi.org/10.1016/j.memsci.2019.02.049.

[11] P. Dydo, M. Turek, J. Ciba, K. Wandachowicz, J. Misztal, The nucleation kinetic aspects of gypsum nanofiltration membrane scaling, Desalination 164 (1) (2004) 41–52, https://doi.org/10.1016/S0011-9164(04)00154-7.

[12] A. Packter, The precipitation of calcium sulphate dihydrate from aqueous solution, J. Cryst. Growth 21 (2) (1974) 191–194, https://doi.org/10.1016/0022-0248(74)90004-9.

[13] M. Rezaei, D.M. Warsinger, V.J.H. Lienhard, M.C. Duke, T. Matsuura, W. M. Samhaber, Wetting phenomena in membrane distillation: mechanisms, reversal, and prevention, Water Res. 139 (2018) 329–352, https://doi.org/10.1016/j.watres.2018.03.058.

[14] Y. Chen, K.J. Lu, T.S. Chung, An omniphobic slippery membrane with simultaneous anti-wetting and anti-scaling properties for robust membrane distillation, J. Membr. Sci. 2020 (595) (September 2019), 117572, https://doi.org/10.1016/j.memsci.2019.117572.

[15] D.M. Warsinger, J. Swaminathan, E. Guillen-Burrieza, H.A. Arafat, V.J.H. Lienhard, Scaling and fouling in membrane distillation for desalination applications: a review, Desalination 356 (2015) 294–313, https://doi.org/10.1016/j.desal.2014.06.031.

[16] P. Zhang, P. Knötig, S. Gray, M. Duke, Scale reduction and cleaning techniques during direct contact membrane distillation of seawater reverse osmosis brine, Desalination 374 (2015) 20–30, https://doi.org/10.1016/j.desal.2015.07.005.

[17] F. He, K.K. Sirkar, J.L. Gilron, Effects of antiscalants to mitigate membrane scaling by direct contact membrane distillation, J. Membr. Sci. 345 (1–2) (2009) 53–58, https://doi.org/10.1016/j.memsci.2009.08.021.

[18] M. Gryta, Calcium sulphate scaling in membrane distillation process, Chem. Pap. 63 (2) (2009) 146–151, https://doi.org/10.2478/s11696-008-0095-y.

[19] Y. Peng, J. Ge, Z. Li, S. Wang, Effects of anti-scaling and cleaning chemicals on membrane scale in direct contact membrane distillation process for RO brine concentrate, Sep. Purif. Technol. 154 (2015) 22–26, https://doi.org/10.1016/j.seppur.2015.09.007.

[20] W. Yu, D. Song, W. Chen, H. Yang, Antiscalants in RO membrane scaling control, Water Res. 183 (2020), 115985, https://doi.org/10.1016/j.watres.2020.115985.

[21] Y. Yin, N. Jeong, R. Minjarez, C.A. Robbins, K.H. Carlson, T. Tong, Contrasting behaviors between gypsum and silica scaling in the presence of antiscalants during membrane distillation, Environ. Sci. Technol. (2021), https://doi.org/10.1021/acs.est.0c07190.

[22] D. Hasson, A. Cornel, Effect of residence time on the degree of CaCO3 precipitation in the presence of an anti-scalant, Desalination 401 (2017) 64–67, https://doi.org/10.1016/j.desal.2016.06.006.

[23] T. Horseman, C. Su, K.S.S. Christie, S. Lin, Highly effective scaling mitigation in membrane distillation using a superhydrophobic membrane with gas purging, Environ. Sci. Technol. Lett. 6 (7) (2019) 423–429, https://doi.org/10.1021/acs.estlett.9b00354.

[24] K.L. Hickenbottom, T.Y. Cath, D.K. Pannell, J. Poe, C.R. Milne, Methods for Sustainable Membrane Distillation Concentration of Hypersaline Streams, 2016.

[25] C. Su, T. Horseman, H. Cao, Y. Li, S. Lin, K.S.S. Christie, Y. Li, S. Lin, Robust superhydrophobic membrane for membrane distillation with excellent scaling resistance, Environ. Sci. Technol. (2019), https://doi.org/10.1021/acs.est.9b04362.

[26] T. Horseman, Y. Yin, K.S.S. Christie, Z. Wang, T. Tong, S. Lin, Wetting, scaling, and fouling in membrane distillation: state-of-the-art insights on fundamental mechanisms and mitigation strategies, ACS ES&T Eng. 1 (1) (2021) 117–140, https://doi.org/10.1021/acsestengg.0c00025.

[27] Y. Yin, N. Jeong, T. Tong, The effects of membrane surface wettability on pore wetting and scaling reversibility associated with mineral scaling in membrane distillation, J. Membr. Sci. 614 (May) (2020), 118503, https://doi.org/10.1016/j.memsci.2020.118503.

[28] Y. Yin, W. Wang, A.K. Kota, S. Zhao, T. Tong, Elucidating mechanisms of silica scaling in membrane distillation: effects of membrane surface wettability, Environ. Sci. Water Res. Technol. 5 (11) (2019) 2004–2014, https://doi.org/10.1039/c9ew00626e.

[29] R. Zheng, H. Yin, Y. Liu, H. He, Y. Zhang, X.-M. Li, Y. Ji, Z. Xiao, X. Yuan, T. He, D. Li, Slippery for scaling resistance in membrane distillation: a novel porous micropillared superhydrophobic surface, Water Res. 155 (2019) 152–161, https://doi.org/10.1016/j.watres.2019.01.036.

[30] L. Liu, Z. Xiao, Y. Liu, X. Li, H. Yin, A. Volkov, T. He, Understanding the fouling/scaling resistance of superhydrophobic/omniphobic membranes in membrane distillation, Desalination 2021 (499) (November 2020), 114864, https://doi.org/10.1016/j.desal.2020.114864.

[31] Z. Xiao, Z. Li, H. Guo, Y. Liu, Y. Wang, H. Yin, X. Li, J. Song, L.D. Nghiem, T. He, Scaling mitigation in membrane distillation: from superhydrophobic to slippery, Desalination 466 (May) (2019) 36–43, https://doi.org/10.1016/j.desal.2019.05.006.

[32] J.A. Bush, J. Vanneste, T.Y. Cath, Membrane distillation for concentration of hypersaline brines from the great salt Lake: effects of scaling and fouling on performance, efficiency, and salt rejection, Sep. Purif. Technol. 170 (2016) 78–91, https://doi.org/10.1016/j.seppur.2016.06.028.

[33] L. Liu, H. He, Y. Wang, T. Tong, X. Li, Y. Zhang, T. He, Mitigation of gypsum and silica scaling in membrane distillation by pulse flow operation, J. Membr. Sci. 2021 (624) (December 2020), 119107, https://doi.org/10.1016/j.memsci.2021.119107.

[34] A.L. McGaughey, R.D. Gustafson, A.E. Childress, Effect of long-term operation on membrane surface characteristics and performance in membrane distillation,

J. Membr. Sci. 543 (August) (2017) 143–150, https://doi.org/10.1016/j.memsci.2017.08.040.

[35] Y. Xu, Y. Liao, Z. Lin, J. Lin, Q. Li, J. Lin, Z. Jin, Precipitation of calcium sulfate dihydrate in the presence of fulvic acid and magnesium ion, Chem. Eng. J. 361 (January) (2019) 1078–1088, https://doi.org/10.1016/j.cej.2019.01.003.

[36] D.M. Warsinger, J. Swaminathan, E. Guillen-Burrieza, H.A. Arafat, V.J.H. Lienhard, Scaling and fouling in membrane distillation for desalination applications: a review, Desalination 356 (2015) 294–313, https://doi.org/10.1016/j.desal.2014.06.031.

[37] A. Antony, J.H. Low, S. Gray, A.E. Childress, P. Le-Clech, G. Leslie, Scale formation and control in high pressure membrane water treatment systems: a review, J. Membr. Sci. 383 (1–2) (2011) 1–16, https://doi.org/10.1016/j.memsci.2011.08.054.

[38] L.F. Greenlee, D.F. Lawler, B.D. Freeman, B. Marrot, P. Moulin, Reverse osmosis desalination: water sources, technology, and Today's challenges, Water Res. 43 (9) (2009) 2317–2348, https://doi.org/10.1016/j.watres.2009.03.010.

[39] Y.A. Le Gouellec, M. Elimelech, Calcium sulfate (Gypsum) scaling in nanofiltration of agricultural drainage water, J. Membr. Sci. 205 (1–2) (2002) 279–291, https://doi.org/10.1016/S0376-7388(02)00128-X.

[40] M. Gryta, Calcium sulphate scaling in membrane distillation process, Chem. Pap. 63 (2) (2009) 146–151, https://doi.org/10.2478/s11696-008-0095-y.

[41] A. Anvari, K.M. Kekre, A. Ronen, Scaling mitigation in radio-frequency induction heated membrane distillation, J. Membr. Sci. 2020 (600) (November 2019), 117859, https://doi.org/10.1016/j.memsci.2020.117859.

[42] L.D. Nghiem, T. Cath, A scaling mitigation approach during direct contact membrane distillation, Sep. Purif. Technol. 80 (2) (2011) 315–322, https://doi.org/10.1016/j.seppur.2011.05.013.

[43] K.W. Lawson, D.R. Lloyd, Membrane distillation, J. Memb. Sci. 124 (1) (1997) 1–25, https://doi.org/10.1016/S0376-7388(96)00236-0.

[44] M. Khayet, T. Matsuura, Membrane Distillation: Principles and Applications, 2011.

[45] M. Qtaishat, T. Matsuura, B. Kruczek, M. Khayet, Heat and mass transfer analysis in direct contact membrane distillation, Desalination 219 (1–3) (2008) 272–292, https://doi.org/10.1016/j.desal.2007.05.019.

[46] M. Gryta, Fouling in direct contact membrane distillation process, J. Membr. Sci. 325 (1) (2008) 383–394, https://doi.org/10.1016/j.memsci.2008.08.001.

[47] D.M. Warsinger, E.W. Tow, J. Swaminathan, V.J.H. Lienhard, Theoretical framework for predicting inorganic fouling in membrane distillation and experimental validation with calcium sulfate, J. Membr. Sci. 2017 (528) (November 2016) 381–390, https://doi.org/10.1016/j.memsci.2017.01.031.

[48] M.E. Leitch, G.V. Lowry, M.S. Mauter, Characterizing convective heat transfer coefficients in membrane distillation cassettes, J. Membr. Sci. 538 (May) (2017) 108–121, https://doi.org/10.1016/j.memsci.2017.05.028.

[49] J. Phattaranawik, R. Jiraratananon, A.G. Fane, Heat transport and membrane distillation coefficients in direct contact membrane distillation, J. Membr. Sci. 212 (1–2) (2003) 177–193, https://doi.org/10.1016/S0376-7388(02)00498-2.

[50] O.R. Lokare, R.D. Vidic, Impact of operating conditions on measured and predicted concentration polarization in membrane distillation, Environ. Sci. Technol. 53 (2019) 11869–11876, https://doi.org/10.1021/acs.est.9b04182.

[51] I. Hitsov, L. Eykens, W.De Schepper, K.De Sitter, C. Dotremont, I. Nopens, Full-scale direct contact membrane distillation (DCMD) model including membrane compaction effects, J. Membr. Sci 524 (September 2016) (2017) 245–256, https://doi.org/10.1016/j.memsci.2016.11.044.

[52] J. W. Gibbs On the equilibrium of heterogeneous substances. Trans. Connect. Acad. Arts Sci. 3, 108–248 and 343–524.

[53] P.G. Vekilov, Nucleation, Cryst. Growth Des. 10 (12) (2010) 5007–5019, https://doi.org/10.1021/cg1011633.

[54] J.J. De Yoreo, P.G. Vekilov, Principles of crystal nucleation and growth, Rev. Mineral. Geochem. 54 (1) (2003) 57–93, https://doi.org/10.2113/0540057.

[55] G.C. Sosso, J. Chen, S.J. Cox, M. Fitzner, P. Pedevilla, A. Zen, A. Michaelides, Crystal nucleation in liquids: open questions and future challenges in molecular dynamics simulations, Chem. Rev. 116 (12) (2016) 7078–7116, https://doi.org/10.1021/acs.chemrev.5b00744.

[56] M. Perez, Gibbs-Thomson effects in phase transformations, Scr. Mater. 52 (8) (2005) 709–712, https://doi.org/10.1016/j.scriptamat.2004.12.026.

[57] D. Kashchiev, Driving force for nucleation, Nucleation (2000) 9–16, https://doi.org/10.1016/b978-075064682-6/50003-2.

[58] W.L. Marshall, R. Slusher, Aqueous systems at high temperature: solubility to 200° C. of calcium sulfate and its hydrates in sea water and saline water concentrates, and temperature-concentration limits, J. Chem. Eng. Data 13 (1) (1968) 83–93, https://doi.org/10.1021/je60036a027.

[59] A. Hina, G.H. Nancollas, Precipitation and dissolution of alkaline earth sulfates: kinetics and surface energy, Rev. Mineral. Geochem. 40 (4) (2000) 276–301, https://doi.org/10.2138/rmg.2000.40.5.

[60] X.Y. Liu, Heterogeneous nucleation or homogeneous nucleation? J. Chem. Phys. 112 (22) (2000) 9949–9955, https://doi.org/10.1063/1.481644.

[61] M. Xie, S.R. Gray, Silica scaling in forward osmosis: from solution to membrane Interface, Water Res. 108 (2017) 232–239, https://doi.org/10.1016/j.watres.2016.10.082.

[62] B. Cao, A. Ansari, X. Yi, D.F. Rodrigues, Y. Hu, Gypsum scale formation on graphene oxide modified reverse osmosis membrane, J. Membr. Sci. 552 (February) (2018) 132–143, https://doi.org/10.1016/j.memsci.2018.02.005.

[63] D. Turnbull, Kinetics of heterogeneous nucleation, J. Chem. Phys. 18 (2) (1950) 198–203, https://doi.org/10.1063/1.1747588.

[64] H.J. Maris, Introduction to the physics of nucleation, C. R. Phys. 7 (9–10) (2006) 946–958, https://doi.org/10.1016/j.crhy.2006.10.019.

[65] M. Förster, M. Bohnet, Influence of the interfacial free energy crystal/heat transfer surface on the induction period during fouling, Int. J. Therm. Sci. 38 (11) (1999) 944–954, https://doi.org/10.1016/S1290-0729(99)00102-7.

[66] J.H. ter Horst, C. Schmidt, J. Ulrich, Fundamentals of Industrial Crystallization Second Edi., Vol. 2, Elsevier B.V, 2015 https://doi.org/10.1016/B978-0-444-63303-3.00032-8.

[67] E. Curcio, E. Fontananova, G. Di Profio, E. Drioli, Influence of the structural properties of Poly(Vinylidene Fluoride) membranes on the heterogeneous nucleation rate of protein crystals, J. Phys. Chem. B 110 (25) (2006) 12438–12445, https://doi.org/10.1021/jp061531y.

[68] E. Curcio, X. Ji, G. Di Profio, A.O. Sulaiman, E. Fontananova, E. Drioli, Membrane distillation operated at high seawater concentration factors: role of the membrane on CaCO3 scaling in presence of humic acid, J. Membr. Sci. 346 (2) (2010) 263–269, https://doi.org/10.1016/j.memsci.2009.09.044.

[69] C.J. Van Oss, M.K. Chaudhury, R.J. Good, Interfacial Lifshitz-van Der Waals and polar interactions in macroscopic systems, Chem. Rev. 88 (6) (1988) 927–941, https://doi.org/10.1021/cr00088a006.

[70] W.L. Marshall, R. Slusher, Thermodynamics of calcium sulfate dihydrate in aqueous sodium chloride solutions, 0–110°, J. Phys. Chem. 70 (12) (1966) 4015–4027, https://doi.org/10.1021/j100884a044.

[71] D. Barba, V. Brandani, G. di Giacomo, A thermodynamic model of CaSO4 solubility in multicomponent aqueous solutions, Chem. Eng. J. 24 (2) (1982) 191–200, https://doi.org/10.1016/0300-9467(82)80034-8.

[72] J. Budz, A.G. Jones, J.W. Mullin, Effect of selected impurities on the continuous precipitation of calcium sulphate (Gypsum), J. Chem. Technol. Biotechnol. 36 (4) (1986) 153–161, https://doi.org/10.1002/jctb.280360402.

[73] K.G. Nayar, M.H. Sharqawy, L.D. Banchik, J.H. Lienhard, Thermophysical properties of seawater: a review and new correlations that include pressure dependence, Desalination 390 (2016) 1–24, https://doi.org/10.1016/j.desal.2016.02.024.

[74] F. Ahmi, A. Gadri, Kinetics and morphology of formed gypsum, Desalination 166 (1–3) (2004) 427–434, https://doi.org/10.1016/j.desal.2004.06.097.

[75] P.G. Klepetsanis, E. Dalas, P.G. Koutsoukos, Role of temperature in the spontaneous precipitation of calcium sulfate dihydrate, Langmuir 15 (4) (1999) 1534–1540, https://doi.org/10.1021/la9800912.

[76] L. Song, B. Li, K.K. Sirkar, J.L. Gilron, Direct contact membrane distillation-based desalination: novel membranes, devices, larger-scale studies, and a model, Ind. Eng. Chem. Res. 46 (8) (2007) 2307–2323, https://doi.org/10.1021/ie0609968.

[77] L. Song, Z. Ma, X. Liao, P.B. Kosaraju, J.R. Irish, K.K. Sirkar, Pilot plant studies of novel membranes and devices for direct contact membrane distillation-based desalination, J. Membr. Sci. 323 (2) (2008) 257–270, https://doi.org/10.1016/j.memsci.2008.05.079.

[78] S. Adham, A. Hussain, J.M. Matar, R. Dores, A. Janson, Application of membrane distillation for desalting brines from thermal desalination plants, Desalination 314 (2013) 101–108, https://doi.org/10.1016/j.desal.2013.01.003.

[79] B. Mi, M. Elimelech, Gypsum scaling and cleaning in forward osmosis: measurements and mechanisms, Environ. Sci. Technol. 44 (6) (2010) 2022–2028, https://doi.org/10.1021/es903623r.

[80] F. Alimi, H. Elfil, A. Gadri, Kinetics of the precipitation of calcium sulfate dihydrate in a desalination unit, Desalination 158 (1–3) (2003) 9–16, https://doi.org/10.1016/S0011-9164(03)00426-0.

[81] F. He, J. Gilron, H. Lee, L. Song, K.K. Sirkar, Potential for scaling by sparingly soluble salts in crossflow DCMD, J. Membr. Sci. 311 (1–2) (2008) 68–80, https://doi.org/10.1016/j.memsci.2007.11.056.

[82] M. Prisciandaro, A. Lancia, D. Musmarra, Calcium sulfate dihydrate nucleation in the presence of calcium and sodium chloride salts, Ind. Eng. Chem. Res. 40 (10) (2001) 2335–2339, https://doi.org/10.1021/ie000391q.

[83] D.M. Warsinger, A. Servi, S. Van Belleghem, J. Gonzalez, J. Swaminathan, J. Kharraz, H.W. Chung, H.A. Arafat, K.K. Gleason, V.J.H. Lienhard, Combining air recharging and membrane superhydrophobicity for fouling prevention in membrane distillation, J. Membr. Sci. 505 (2016) 241–252, https://doi.org/10.1016/j.memsci.2016.01.018.

[84] A. Hina, G.H. Nancollas, M. Grynpas, Surface induced constant composition crystal growth kinetics studies. The Brushite-Gypsum System, J. Cryst. Growth 223 (1–2) (2001) 213–224, https://doi.org/10.1016/S0022-0248(00)01026-5.